DOI: 10.61782/fa.2023.0019

forumacusticum 2023

POST-PROCESSING FLOWS USING PHYSICS-INFORMED NEURAL NETWORKS

Stefan Schoder[1,*], **Florian Kraxberger**[1], **Eniz Mušeljić**[1], **Andreas Wurzinger**[1]
[1] Institute of Fundamentals and Theory in Electrical Engineering (IGTE),
Graz University of Technology, Graz, Austria

ABSTRACT

In this contribution, the Helmholtz decomposition of a compressible flow velocity field into vortical and compressible structures is implemented using a finite element framework and physics-informed neural networks. These two implementations of Helmholtz's decomposition are compared for a verification example and a 2D mixing layer flow. The work shows how neural networks can leverage physical knowledge to perform the inverse task of post-processing a compressible flow field into subparts. Furthermore, different input variables, network setups, network parameters, network types, and formulations of the objective function for the optimizer are investigated and compared to each other. The physics-informed neural network formulation results on the verification example outline promising directions for further applications to post-process compressible flow fields.

Keywords: *Aeroacoustics, Neural Networks, Physics-Informed Neural Networks*

1. INTRODUCTION

In aeroacoustic modeling, flow and sound's interaction effects and distinct properties have been of great interest [1, 2]. First numerical investigations based on the finite element method to compute the Helmholtz decomposition of high-fidelity compressible aeroacoustic fields were studied in [3, 4]. Therewith, the compressible scalar and vortical vector potentials are uniquely obtained by the used formulation in conjunction with mass regularization and the infinite mapping layer [5]. In general, the Helmholtz decomposition is not unique and poses an inverse problem.

Issue 1: The calculation of Helmholtz's decomposition by solving a set of partial differential equations [4], the so-obtained potentials are not uniquely defined. Further constraints are needed to adequately fulfill the system of equations. In particular, the source term of some wave equations is based on the compressible potential [6] and therefore, uniqueness of the potential is required.

Issue 2: Furthermore, the separation at any boundary is not yet defined by the underlying physical processes. The boundary conditions of the separated potentials are generally expressed in the following way: The mathematical theory suggests that the tangential boundary components are Neumann boundaries of the vortical part. In contrast, the normal vector components at the boundary describe the Neumann boundary for the compressible part. Generally, this assumption at the boundary is oversimplifying. In the discussion of the present article, correlations of the presented flow data were analyzed for a prospective improvement of the boundary condition to enhance the theory of Helmholtz's decomposition in aeroacoustics.

In the present work, the formulation of the newly developed implementation using a physics-informed neural network (PINN) implemented with PyTorch is presented [7, 8]. The PINN implementation incorporates physically-based constraints to address issue 1, and the a-priori data analysis identifies a method to address issue 2. With this information, the existing finite element method implementation can be enhanced in the future. The simulations are applied to a 2D isothermal mixing layer flow [6]. For illustration, a schematic view of the configuration is

*[*] ***Corresponding author**: stefan.schoder@tugraz.at.*

shown in figure 1. This figure shows vortices and their pairings at a period $T_\mathrm{p} = 2\pi/\omega_\mathrm{p} = 2/f$ can be observed at the center of the shear zone. The vortex pairings generate acoustic waves at a frequency $f/2$ in the acoustic field, as seen in figure 1. The mixing layer is centered at $y = 0$ and the velocity $\boldsymbol{u} = [u_x, 0]^\mathrm{T}$ at the inflow boundary condition is given by the hyperbolic-tangent profile

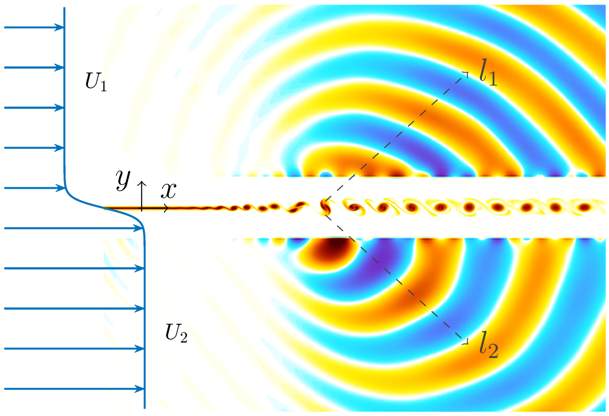

Figure 1. Schematic view of the mixing layer and the three evaluation lines of the results. Instantaneous vorticity and fluctuating pressure fields are represented at the shear zone's center and periphery.

$$u_x(y) = \frac{U_1 + U_2}{2} - \frac{U_2 - U_1}{2} \tanh\left(\frac{2y}{\delta_\omega}\right) \qquad (1)$$

where $U_1 = 0.3c_0$ and $U_2 = 0.6c_0$ are the velocities of the slow and rapid flows, respectively, and $\delta_\omega = (U_2 - U_1)/\max(|\mathrm{du_x/dy}|)$ is the vorticity thickness at the upstream boundary which provides a Reynolds number of $Re_\omega = \delta_\omega(U_2 - U_1)/\nu = 2000$, where ν is the kinematic viscosity and c_0 is the speed of sound.

The paper is organized as follows. In sec. 2, we will describe the fundamentals of Helmholtz's decomposition, its PINNs implementation, training, and verification. Section 3 describes the benchmark against an implementation using the finite element method. The following sec. 4 describes the results applied to the mixing layer problem. Finally, the paper is concluded in sec. 5.

2. NEURAL NETWORK, TRAINING AND VERIFICATION

The neural network is set up in different variants and verified accordingly. In general, when calculating the Helmholtz decomposition, an equation for the scalar potential (compressible part) and one for the vector potential (vortical part) is solved. The compressible part of Helmholtz's decomposition is the solution of the inhomogeneous Neumann problem

$$\nabla \cdot \nabla\phi = \nabla \cdot \boldsymbol{u}' \,, \qquad (2)$$

with $\boldsymbol{n} \cdot \nabla\phi = \boldsymbol{n} \cdot \boldsymbol{u}_\mathrm{c}$. In 2D, the vortical part of Helmholtz's decomposition on a concave domain is the solution of the inhomogeneous Neumann problem

$$-\nabla \cdot \nabla(\boldsymbol{A} \cdot \boldsymbol{e}_z) = \nabla \times \boldsymbol{u}' \,, \qquad (3)$$

with $\boldsymbol{A} \times \boldsymbol{n} = \boldsymbol{u}_\mathrm{v} \times \boldsymbol{n}$.

2.1 Network and objective function type

Fully connected layers define the neural network with later specified width and depth. Two different cost function types are used to define (i) a segregated and (ii) a monolithic HelmholtzNet. The segregated HelmholtzNet consists of two neural nets, where one models the scalar potential part and the other the vector potential part. Within the monolithic framework, both equations are satisfied by one neural network.

2.1.1 Segregated HelmholtzNet

This section's PINN loss function is modified to comply with the individual decomposition equations used to obtain the analytical solution in Tab. 1 and Tab. 2. In this sense, the loss function of the scalar potential PINN is

$$\begin{aligned} L(x,y) = {} & \frac{1}{N_\mathrm{pde}} \sum_{i=1}^{N_\mathrm{pde}} \left[\nabla \cdot \nabla\phi_i - \nabla \cdot \boldsymbol{u}'(x_i, y_i)\right]^2 \\ & + \frac{1}{N_\mathrm{pde,bc}} \sum_{l=1}^{N_\mathrm{pde,bc}} \left[((\nabla\phi_l) \cdot \boldsymbol{n}\right]^2 \,, \end{aligned} \qquad (4)$$

with $N_\mathrm{pde,bc}$ being the number of boundary points and $\boldsymbol{n}$ the normal of the boundary. The loss function of the vector potential PINN reads as

$$\begin{aligned} L(x,y) = {} & \frac{1}{N_\mathrm{pde}} \sum_{i=1}^{N_\mathrm{pde}} \left[\nabla \cdot \nabla(\boldsymbol{A}_i \cdot \boldsymbol{e}_z) + \nabla \times \boldsymbol{u}'(x_i, y_i)\right]^2 \\ & + \frac{1}{N_\mathrm{pde,bc,h}} \sum_{l=1}^{N_\mathrm{pde,bc,h}} \left[((\nabla \times \boldsymbol{A}_l) \times \boldsymbol{n}\right]^2 \\ & + \frac{1}{N_\mathrm{pde,bc,ih}} \sum_{l=1}^{N_\mathrm{pde,bc,ih}} \left[((\nabla \times \boldsymbol{A}_l) \times \boldsymbol{n} - \boldsymbol{u}'(x_l, y_l) \times \boldsymbol{n}\right]^2 \,, \end{aligned} \qquad (5)$$

with $N_{\mathrm{pde,bc,h}}$ being the number of boundary points of the homogeneous boundary condition and $N_{\mathrm{pde,bc,ih}}$ the number of boundary points of the inhomogeneous boundary condition. It is important to note that both of these cost functions supply some hidden information at the boundaries where

$$\boldsymbol{n} \cdot (\nabla\nabla \cdot \boldsymbol{u}') \neq 0 \tag{6}$$

for time t.

2.1.2 *Monolithic HelmholtzNet*

Within this section, the monolithic HelmholtzNet is derived based on the coupling cost function and getting rid of the supplied hidden information to the network. In this sense, the following cost function is obtained

$$\begin{aligned} L(x,y) = {} & \frac{1}{N_{\mathrm{pde}}} \sum_{i=1}^{N_{\mathrm{pde}}} \left[\nabla \cdot \nabla \phi_i - \nabla \cdot \boldsymbol{u}'(x_i, y_i)\right]^2 \\ & + \frac{1}{N_{\mathrm{pde,bc}}} \sum_{l=1}^{N_{\mathrm{pde,bc}}} \left[((\nabla \phi_l) \cdot \boldsymbol{n}\right]^2 \\ & + \frac{1}{N_{\mathrm{pde}}} \sum_{j=1}^{N_{\mathrm{pde}}} \left[\nabla \cdot \nabla(\boldsymbol{A}_j \cdot \boldsymbol{e}_z) + \boldsymbol{\omega}_{\mathrm{z}}'(x_j, y_j)\right]^2 \\ & + \frac{1}{N_{\mathrm{pde,bc}}} \sum_{l=1}^{N_{\mathrm{pde,bc}}} \left[((\nabla \times \boldsymbol{A}_l) \times \boldsymbol{n}\right]^2 \\ & + \left[\frac{1}{N_{\mathrm{pde}}} \sum_{l=1}^{N_{\mathrm{pde}}} (\nabla \times \boldsymbol{A}_l) \cdot (\nabla \phi_l)\right]^2 \\ & + \frac{1}{N_{\mathrm{pde}}} \sum_{m=1}^{N_{\mathrm{pde}}} \left[\nabla \times \boldsymbol{A}_m + \nabla \phi_l - \boldsymbol{u}'(x_m, y_m)\right]^2 \\ & + \epsilon \frac{1}{N_{\mathrm{pde}}} \sum_{m=1}^{N_{\mathrm{pde}}} \left[\nabla \times \boldsymbol{A}_m\right]^2 + \epsilon \frac{1}{N_{\mathrm{pde}}} \sum_{m=1}^{N_{\mathrm{pde}}} \left[\nabla \phi_l\right]^2 , \end{aligned} \tag{7}$$

with the last two terms minimizing the vortical and the compressible energy content of the obtained fields. $N_{\mathrm{pde,bc,const}}$ is the number of boundary points where $\boldsymbol{n} \cdot (\nabla\nabla \cdot \boldsymbol{u}') = 0$ for a timestamp t. The monolithic network is prepared in the same fashion as the segregated PINN, except that the output layer contains two neurons, one for the scalar potential and one for the vector potential, and the number of epochs is increased to 8.000.

2.2 Information and input data

2.2.1 *Data preparation and normalization*

The computational domain coincides with the 2D flow domain of the direct numerical simulation. It uses flow velocity data at collocation points located at the finite difference point coordinates. The loss function is evaluated in these collocation points and is selected according to the monolithic or segregated HelmholtzNet description. In the current version of the HelmholtzNet, no data normalization was applied.

2.2.2 *The HelmholtzNet based on PINN*

The network is set up according to the PINN setup, either as a segregated net consisting of one output layer neuron or the monolithic net using two neurons, one for the scalar potential and one for the vector potential. In this case, the auto-differentiation algorithms of the neural network can be used to determine the necessary derivatives for the partial differential equation constraints.

2.2.3 *The HelmholtzNet using additional information*

The network is modified such that the input layer is supplied with additional data: besides

$$\{x, y\}$$

also

$$\{\boldsymbol{u}',\, \nabla \cdot \boldsymbol{u}',\, \nabla \times \boldsymbol{u}'\}$$

are given as input information. This results in $2 + N_{\mathrm{i}}$ neurons for the input layer, where N_{i} is the number of neurons taking care of additional information provided. The network with additional information uses a hidden layer with a total number of $N_{\mathrm{pde}} + N_{\mathrm{i}}$ neurons. In this case, the derivatives of the network are implemented by the gradient function for non-uniform grid spacing on multi-dimensions.

2.3 Network specifications

The network has the following structure of fully connected linear layers: The input layer takes the $2 + N_{\mathrm{i}}$ dimensions as data input. This input layer is fully connected to the next layer consisting of

$$\mathrm{floor}(2\sqrt{N_{\mathrm{pde}}}) \tag{8}$$

neurons. In total, a number of

$$\mathrm{floor}(\sqrt{N_{\mathrm{pde}}}/2) \tag{9}$$

hidden layers are used. The output layer of the segregated network has one output for either the scalar potential (scalar potential PINN) or the vector potential (vector potential PINN). In contrast to that, the monolithic net has two outputs. The sequential layers have a tangent-hyperbolic activation function. The stopping criteria of the used *Limited-memory Broyden–Fletcher–Goldfarb–Shanno* (LBFGS) algorithm are set to 3000 epochs, or 50000 function evaluations, depending on which one is satisfied first. *Kaiming He* initialization is used to initialize the network [9]. The training was conducted on an AMD Ryzen 7 PRO 5850U processor with 1.9 GHz.

2.4 Analytic benchmark

This analytic example of Helmholtz's decomposition serves as a verification of the PINN implementation in PyTorch [10]. A velocity field of the form

$$\begin{aligned}\boldsymbol{u} = &\,(u_0 + \sin(\pi x)\cos(\omega t) - y\cos(\omega t))\boldsymbol{e}_x \\ &+ x\cos(\omega t)\boldsymbol{e}_y\end{aligned}$$

is prescribed on the domain $\Omega = [0,2]^2$. The mean velocity field is not subject to decomposition $\langle \boldsymbol{u} \rangle = u_0 \boldsymbol{e}_x$. The fluctuating velocity field comes with a vorticity distribution of

$$\boldsymbol{\omega}' = \nabla \times \boldsymbol{u}' = 2\cos(\omega t)\boldsymbol{e}_z$$

and a dilatation of

$$\nabla \cdot \boldsymbol{u}' = \pi \cos(\pi x)\cos(\omega t).$$

The compressible part of Helmholtz's decomposition is the solution of the inhomogeneous Neumann problem (2). The solution

$$\boldsymbol{u}_\mathrm{c} = \nabla \phi$$

and the conjugated field

$$\boldsymbol{u}_\mathrm{v}^* = \boldsymbol{u} - \boldsymbol{u}_\mathrm{c} = \boldsymbol{u} - \nabla \phi$$

are L_2-orthogonal. The obtained solution is given in Tab. 1 with further details provided in [11]. Performing the procedure for the vortical part of Helmholtz's decomposition $\boldsymbol{u}_\mathrm{v}$ as given in (3), the analytic results are obtained and reported in Tab. 2. The FEM-based solution and the comparison to the analytic solution are reported in [3]. In the next step, the performance of the various PINN implementations is evaluated and compared to the preliminary results of [11].

Table 1. Helmholtz's decomposition - The compressible part of the velocity, based on the scalar potential at $t = 0$ [11].

Scalar potential	**Complementary field**
$\phi = -\frac{1}{\pi}\cos(\pi x)$	
$\boldsymbol{u}_\mathrm{c} = \sin(\pi x)\boldsymbol{e}_x$	$\boldsymbol{u}_\mathrm{v}^* = \boldsymbol{u}' - \boldsymbol{u}_\mathrm{c} = -y\boldsymbol{e}_x + x\boldsymbol{e}_y$

Table 2. Helmholtz's decomposition - The incompressible part of the velocity, based on the vector potential at $t = 0$ [11].

Vector potential	**Complementary field**
$A_z = -\frac{1}{2}y^2 - \frac{1}{2}x^2$	
$\boldsymbol{u}_\mathrm{v} = -y\boldsymbol{e}_x + x\boldsymbol{e}_y$	$\boldsymbol{u}_\mathrm{c}^* = \boldsymbol{u}' - \boldsymbol{u}_\mathrm{v} = \sin(\pi x)\boldsymbol{e}_x$

2.5 Verification

Inside the decomposition domain, the number of training data points of the neural network are varied systematically from the set

$$N_\mathrm{pde} \in \{10, 20, 40, 80\}$$

and the results are reported. The two objective function types (segregated and monolithic) are studied. Furthermore, the use of additional information as network input is enriched in two steps, firstly adding the respective right-hand-sides $\nabla \cdot \boldsymbol{u}'$ and $\nabla \times \boldsymbol{u}'$, and secondly the underlying flow field $\boldsymbol{u}'$. This step is only carried out for the monolithic network. In total, this comprises 16 different network configurations.

2.5.1 *Accuracy and Performance of the segregated and monolithic HelmholtzNet*

The relative mean squared error (MSE) of the PINN to the analytic solution

$$e = \frac{\sum_{i=1}^{N_\mathrm{pde}} [\| \boldsymbol{u}_\mathrm{PINN} - \boldsymbol{u}_\mathrm{ANA} \|_2]^2}{\sum_{i=1}^{N_\mathrm{pde}} [\| \boldsymbol{u}_\mathrm{ANA} \|_2]^2} \qquad (10)$$

where $\boldsymbol{u}_\mathrm{PINN}$ is the solution of the PINN, $\boldsymbol{u}_\mathrm{ANA}$ the result of the analytic solution, and $\| \ \boldsymbol{u}_\mathrm{ANA} \ \|_2$ the L_2 norm of the velocity. Based on this, the following errors are determined and reported in Tab. 3 for the segregated HelmholtzNet, and in Tab. 4 for the monolithic HelmholtzNet. Both networks are supplied with input (x, y) and implemented using PyTorch. With increasing resolution, the error drops accordingly.

Table 3. The relative MSE from the segregated HelmholtzNet with input (x, y) in PyTorch [11].

	Error of compressible part			**Error of vortical part**		
N	Training time	Training loss	Error	Training time	Training loss	Error
10	1.86s	8.86e-06	0.1183%	1.05s	3.09e-06	0.0324%
20	1.73s	4.25e-06	0.1096%	2.77s	1.04e-06	0.0218%
40	8.53s	1.69e-06	0.0850%	4.71s	6.89e-07	0.0214%
80	44.55s	1.14e-06	0.0415%	33.78s	8.93e-07	0.0196%

Table 4. The relative MSE from the monolithic HelmholtzNet with input (x, y) in PyTorch [11].

N	**Error of compressible part**	**Error of vortical part**	**Training time**	**Training loss**
10	0.403%	0.190%	2.96s	7.817e-04
20	0.249%	0.099%	12.00s	6.902e-05
40	0.095%	0.059%	45.98s	1.894e-05
80	0.081%	0.047%	169.99s	1.451e-05

2.5.2 Accuracy and Performance of the monolithic HelmholtzNet with additional input information

Within this section, the performance of the monolithic HelmholtzNet with additional information as input is discussed. The errors of the compressible and vortical parts are determined by eq. (10) and reported in Tab. 5 and Tab. 6. The error of the vortical and compressible parts decreases with the spatial resolution, and the networks have comparable accuracy.

3. BENCHMARKING METHOD

3.1 Finite element method

First, the finite element implementation in openCFS based on the weak formulation is discussed [12]. In the previous investigation [4], the coupled identification of a unique separation of a vector field in vortical and compressible parts is transformed into two individual equations. This section presents the weak formulation of (i) the individual scalar potential formulation that computes the compressible part, and (ii) the vector potential formulation that computes the vortical part. For further information, the authors refer to [4].

3.1.1 Scalar potential part

Regarding Helmholtz's decomposition, the weak formulation of the scalar potential with mass regularization yields

$$\int_\Omega \nabla\psi \cdot \nabla\phi \, \mathrm{d}x + \underbrace{\int_\Omega \epsilon\psi\phi^\epsilon \, \mathrm{d}x}_{\text{Regularization}} \\ \underbrace{- \int_{\partial\Omega} \psi(\nabla\phi \cdot \boldsymbol{n} \, \mathrm{d}s)}_{\text{Boundary}} = \int_\Omega \psi \nabla \cdot \boldsymbol{u}' \, \mathrm{d}x \, , \tag{11}$$

with ϵ being the regularization factor and ψ the test function. Using this equation, the scalar potential ϕ can be determined uniquely if appropriate boundaries are imposed. In practice, an accurate description of the boundary condition is not known explicitly.

3.1.2 Vector potential part

The weak formulation of the vector potential with mass regularization reads as

$$\int_\Omega (\nabla \times \boldsymbol{A}') \cdot (\nabla \times \boldsymbol{A}) \mathrm{d}x + \underbrace{\int_\Omega \epsilon \boldsymbol{A}' \cdot \boldsymbol{A} \mathrm{d}x}_{\text{Regularization}} \\ \underbrace{- \int_{\partial\Omega} \boldsymbol{A}' \cdot ((\nabla \times \boldsymbol{A}) \times \boldsymbol{n}) \mathrm{d}s}_{\text{Boundary}} = \int_\Omega \boldsymbol{A}' \cdot \boldsymbol{\omega}' \mathrm{d}x \, , \tag{12}$$

Table 5. The relative MSE from the monolithic HelmholtzNet with input $(x, y, \nabla \cdot \boldsymbol{u}', \nabla \times \boldsymbol{u}')$ in PyTorch.

N	**Error of compressible part**	**Error of vortical part**	**Training time**	**Training loss**
10	8.74%	2.65%	25.59s	5.894e-03
20	1.78%	0.85%	25.33s	2.364e-04
40	1.04%	1.39%	25.73	3.092e-04
80	0.66%	0.31%	145.14s	4.005e-05

Table 6. The relative MSE from the monolithic HelmholtzNet with input $(x, y, \nabla \cdot \boldsymbol{u}', \nabla \times \boldsymbol{u}', u'_x, u'_y)$ in PyTorch.

N	**Error of compressible part**	**Error of vortical part**	**Training time**	**Training loss**
10	10.24%	4.49%	12.98s	4.323e-03
20	2.23%	2.37%	46.84	3.170e-04
40	1.81%	3.41%	49.63s	2.314e-04
80	1.14%	1.87%	101.95s	9.130e-05

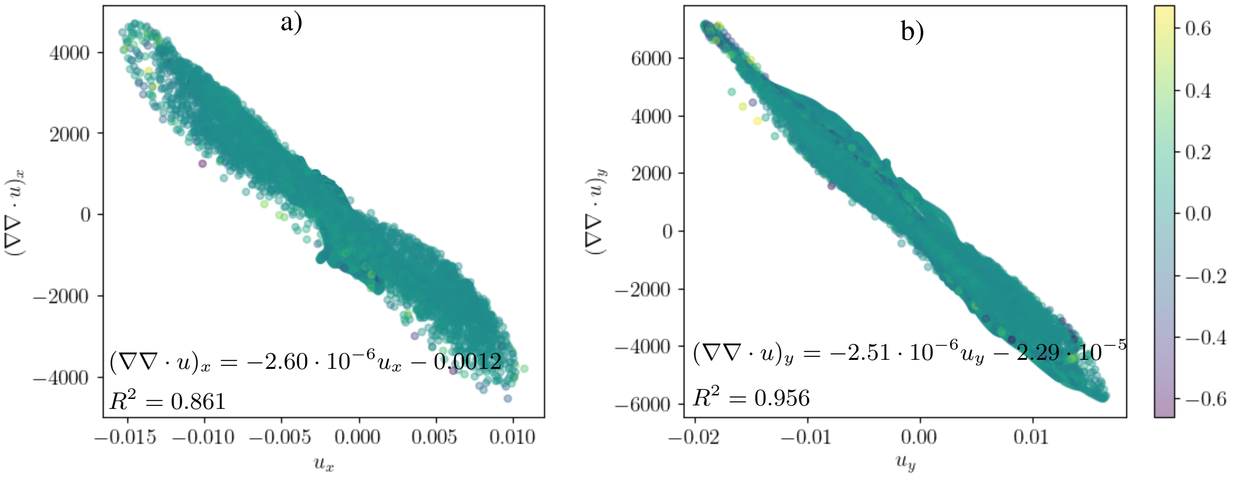

Figure 2. Scattered data plot of the relation between the compressible waves and the gradient of the dilatation on the slow-flow side of the mixing layer.

with $\boldsymbol{A}'$ being the test function. Using this equation, the vector potential $\boldsymbol{A}$ can be determined uniquely if appropriate boundaries are prescribed.

4. MIXING LAYER RESULTS

According to the theory of Helmholtz decomposition, the FEM and PINN methods are applied to a DNS simulation of a mixing layer. First, the DNS field and the simulation input (fluctuating dilatation and vorticity) are analyzed. This is followed by the velocity results obtained by the FEM and PINN implementations. For this work in progress and the application example, only the segregated version of the PINN with additional information predicted reasonable results which are reported here.

4.1 Data analysis and linear predictor

The underlying data was investigated before conducting the machine learning procedures. The data included the following data sets

$$\{x, y, \nabla\times\boldsymbol{u}, \nabla\cdot\boldsymbol{u}, u_x, u_y, |\boldsymbol{u}|,$$
$$(\nabla\nabla\cdot u)_x, (\nabla\nabla\cdot u)_y, |\nabla\times\boldsymbol{u}|\}$$

of the problem to identify possible input features that might be of value for the learning algorithm [8]. By Pearson's correlation, we determined that the correlation factor is -0.92 for $(\nabla\nabla\cdot u)_x, u_x$ and -0.98 for $(\nabla\nabla\cdot u)_y, u_y$. Interestingly, in Fig. 2, it is shown that the gradient of the dilatation has a direct connection to the compressible velocity in regions of low vorticity. This preliminary finding helps to improve the boundary conditions even for the traditional finite element solver solving Helmholtz's decomposition. Based on this correlation, a regression is trained for the data pairs

$$\{u_x, (\nabla\nabla\cdot u)_x\}$$

and

$$\{u_y, (\nabla\nabla\cdot u)_y\}$$

. This simple linear predictor can be used to estimate the compressible velocity within regions of low vorticity. The linear regression estimator was trained on the data of the slow-flow region. Its prediction capabilities were estimated in the region of the rapid flow.

4.2 Line Plots

Figure 3 shows the fluctuating velocity $u_{\mathrm{l}}' = \boldsymbol{u}' \cdot \boldsymbol{n}_{\mathrm{l}}$, the compressible velocity part computed by the FEM implementation $u_{\mathrm{c,l}}^{\mathrm{FEM}} = \boldsymbol{u}_{\mathrm{c}}^{\mathrm{FEM}} \cdot \boldsymbol{n}_{\mathrm{l}}$ and the compressible velocity part calculated by the PINN implementation $u_{\mathrm{c,l}}^{\mathrm{FEM}} = \boldsymbol{u}_{\mathrm{c}}^{\mathrm{FEM}} \cdot \boldsymbol{n}_{\mathrm{l}}$ over the line l_1 and l_2. Line l_1 starts at $(118\delta_\omega, 18\delta_\omega)$ and ends at $(298\delta_\omega, 198\delta_\omega)$. Line l_2 originates at $(118\delta_\omega, -18\delta_\omega)$ and terminates at $(298\delta_\omega, -198\delta_\omega)$. To illustrate the vanishing vortical part in the periphery, the vortical velocity part computed by the FEM implementation is added to Fig. 3. Both the FEM and PINN-based compressible solutions show characteristic acoustic waves and model the compressible solution in regions with low vorticity compared to the mixing region. The two solutions agree with the DNS results in the far field. In addition, the results of the linear regression predictor are added and show good prediction capabilities for Fig. 3a. The generalization of the prediction is assessed by the results of the compressible velocity in Fig. 3b. The main characteristics like the phase and the order of magnitude of the waves are estimated. A slight deviation appears for the positive humps, which are not clear yet.

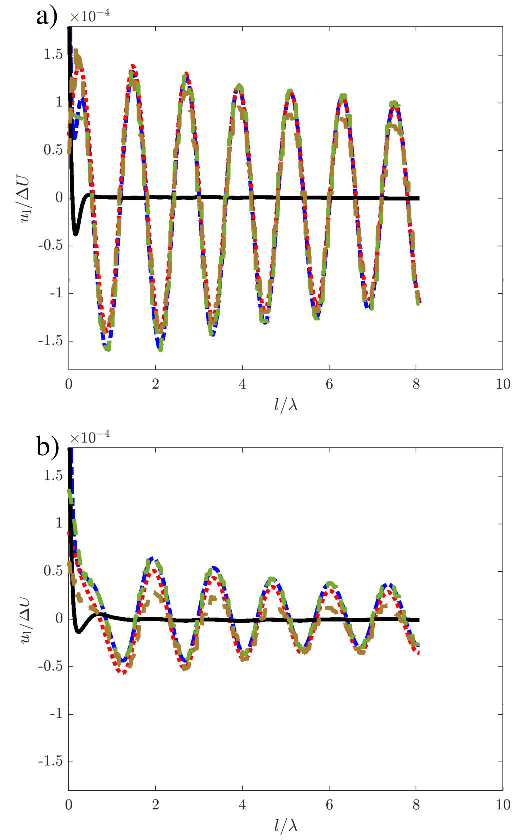

Figure 3. Velocity components a) along the line below the mixing layer and b) the line above the mixing layer. – – u_{l}' of the DNS, ··· $u_{\mathrm{c,l}}^{\mathrm{FEM}}$, —— $u_{\mathrm{c,l}}^{\mathrm{PINN}}$, — — $u_{\mathrm{c,l}}^{\mathrm{LIN}}$ is the prediction based on linear regression, and — $u_{\mathrm{v,l}}^{\mathrm{FEM}}$.

5. CONCLUSION

In this paper, the inverse task of post-processing a compressible subsonic flow field into sub-parts by Helmholtz's decomposition was achieved by different neural network models. Several versions of loss functions and network input combinations are tested. The verification example shows that a PINN algorithm has the potential to perform Helmholtz's decomposition of the flow field with respect to an analytic solution accurately. Previously used decomposition variants presented in [4] and the combined approach (called monolithic HelmholtzNet) show good agreement. It is shown that the monolithic HelmholtzNet has the benefit that it requires less knowledge about the decomposition at the boundary. In addition, the monolithic HelmholtzNet requires a specific implementation of the derivatives.

The presented results from both the verification example and the mixing layer application show promising first results. The benefit of the finite element framework is that it solves the fields directly and mitigates a somewhat tedious optimization process of the inverse problem. Since the presented PINN method does not require information on the decomposition in vortical and compressible effects at the boundaries, the development of acoustic boundaries in fluid dynamics can benefit from these results. A first promising estimate on the compressible flow by a linear regression estimator is presented.

With a direct comparison of the verification examples data and the mixing layer examples data, we identified the following challenges: Firstly, we found that only the HelmholtzNet with additional information was able to achieve reasonable results. Secondly, the mixing layer data has orders of magnitude difference between the compressible and vortical flow fields. Until now, only the segregated HelmholtzNet is capable of predicting the separated flow field. Fourthly, the field patterns are localized, of the same spatial wavelength, and therefore relatively easy to predict by general functions. Fifthly, the boundary conditions or constraints for a real-world application example can be automated and based on the temporal mean value of the vorticity relative to the strain rate. Testing these challenging points, the HelmholtzNet is evaluated further in the future. To conclude, the presented formulations help analyze, decompose, and post-process compressible flow fields.

6. ACKNOWLEDGMENTS

Thanks to H. Vincent (Doctoral Candidate at the LMFA in Écully), who provided the flow simulation data of the mixing layer for this investigation. F. K. and A. W. received funding from the FFG under the No. 39480417.

7. REFERENCES

[1] B. Chu and L. S. G. Kovásznay, "Non-linear interactions in a viscous heat-conducting compressible gas," vol. 3, no. 05, pp. 494–514.

[2] A. D. Pierce, *Acoustics: an introduction to its physical principles and applications*. Acoustical Society of America, 1981.

[3] S. Schoder, *Aeroacoustic analogies based on compressible flow data*. PhD thesis, TU Wien, 2019.

[4] S. Schoder, K. Roppert, and M. Kaltenbacher, "Postprocessing of direct aeroacoustic simulations using helmholtz decomposition," *AIAA Journal*, vol. 58, no. 7, pp. 3019–3027, 2020.

[5] S. Schoder, F. Toth, C. Freidhager, and M. Kaltenbacher, "Revisiting infinite mapping layer for open domain problems," *Journal of Computational Physics*, vol. 392, pp. 354–367, 2019.

[6] S. Schoder, M. Kaltenbacher, É. Spieser, H. Vincent, C. Bogey, and C. Bailly, "Aeroacoustic wave equation based on pierce's operator applied to the sound generated by a mixing layer," in *28th AIAA/CEAS Aeroacoustics 2022 Conference*, p. 2896, 2022.

[7] G. E. Karniadakis, I. G. Kevrekidis, L. Lu, P. Perdikaris, S. Wang, and L. Yang, "Physics-informed machine learning," *Nature Reviews Physics*, vol. 3, no. 6, pp. 422–440, 2021.

[8] S. Schoder, A. Wurzinger, and F. Kraxberger, "Computational acoustics," 2022. Lecture Script.

[9] K. He, X. Zhang, S. Ren, and J. Sun, "Delving deep into rectifiers: Surpassing human-level performance on imagenet classification," in *Proc. IEEE International Conference on Computer Vision*, pp. 1026–1034.

[10] S. Schoder, K. Roppert, and M. Kaltenbacher, "Helmholtz's decomposition for compressible flows and its application to computational aeroacoustics," *SN Partial Differential Equations and Applications*, vol. 1, no. 6, pp. 1–20, 2020.

[11] S. Schoder, E. Museljic, F. Kraxberger, and A. Wurzinger, "Post-processing subsonic flows using physics-informed neural networks," in *AIAA AVIATION 2023 Forum*, p. 3340, American Institute of Aeronautics and Astronautics, June 2023.

[12] S. Schoder and K. Roppert, "openCFS: Open source finite element software for coupled field simulation–part acoustics," *arXiv preprint arXiv:2207.04443*, 2022.